CrystEngComm

Accepted Manuscript

ROYAL SOCIETY OF CHEMISTRY

www.rsc.org/crystengcomm

α-Fe_2O_3 Concave and Hollow Nanocrystals: Top-Down Etching Synthesis and Their Comparative Photocatalytic Activities

Pengwei Li,[*] [a] Xiaole Yan,[a] Zaiqian He,[a] Jianlong Ji,[a] Jie Hu,[a] Gang Li,[a] Kun Lian,[b c] Wendong Zhang[a]

Abstract

In this work, the uniform single crystal α-Fe_2O_3 concave and hollow nanocrystals have been synthesized by a facile top-down etching method. Phosphate ions were employed as an etching agent to top-down etch the pristine icositetrahedron along its [006] direction. The etched Fe_2O_3 concave and hollow nanocrystals exhibit a much larger specific surface area (SSA) and more edges, corners and rough structures (hot spots) on the crystal surface compared to their mother crystal, thus serving as the possible origin for their comparative photocatalytic activities on the degradation of cationic dye Rhodamine B. These characters make them the promising candidates for catalysts and sensing materials.

Key words: Hematite; Concave and hollow structures; Top-down etching; Photocatalytic

* To whom correspondence should be addressed. E-mail: lipengwei@tyut.edu.cn.

[a] Micro-Nano System Research Center, College of Information Engineering, Taiyuan University of Technology, Taiyuan 030024, Shanxi, China

[b] Center for Advanced Microstructures and Devices, Louisiana State University, LA 70806, USA

[c] School of Nano-Science and Nano-Engineering, Suzhou & Collaborative Innovation Center of Suzhou Nano Science and Technology, Xi'an Jiaotong University, Xi'an 710049, China

1. Introductions

For most catalytic reactions, it has been shown that high-index planes, which are associated with large numbers of atomic steps, edges, and kinks hold the key to the enhancement of catalytic performance in terms of activity and/or selectivity. [1-8] For example, Tian and co-workers have developed the tetrahexahedral Pt nanocrystals with 24 high-index facets exhibiting much enhanced (up to 400%) catalytic activities toward the electro-oxidations of formic acid and ethanol. [1] Wang et al. synthesized the polyhedral 50-facet Cu_2O microcrystals partially enclosed by {311} high-index planes, which shows enhanced catalytic CO oxidation activity. [3] Nanocrystals with concave or hollow structures also have attracted attention because of their high-active facets. [4, 7-10] To this end, Xia and co-workers have demonstrated the synthesis of concave Pt nanocubes with enhanced activity for oxygen reduction reaction. [4] Zhou et al. reported the $Ni(OH)_2$@$Co(OH)_2$ hollow nanohexagons growth and their superior capacitance property. [7]

Hematite (α-Fe_2O_3), an n-type semiconductor (E_g = 2.1 eV), is a stable form of iron oxides, which has been widely used in many fields such as catalysts, [11, 12] gas sensors, [13, 14] biotechnology, [15-17] and electrode materials. [18, 19] On the basis of its rhombohedral structure (an hexagonal close packing of O atoms with Fe atoms occupying 2/3 of the octahedral sites), [20] α-Fe_2O_3 has been engineered into a wide range of nanostructures, including nano-polyhedrons (cube, octahedral, hexagonal bipyramidal and octadecahedral nanostructures), nanorods, nanospindles, nanorings, nanotubes as well as other hollow and hierarchical nanostructures. [15, 21-27] However, due to the similar surface energies of various low index facets of hematite, the order of stability of surfaces can be changed easily by preferential adsorption of ionic species or slight alterations to reaction conditions. [28] It still remains challenges to produce hematite nanocrystals with high-reactive surfaces by using a facile, scalable route based on hydrothermal method.

In this article, single crystal Fe_2O_3 icositetrahedron has been synthesized first as the mother crystal. Then, a top-down approach has been adopted to fabricate the Fe_2O_3

concave and hexagonal-hollow-ring shaped nanocrystals via a controlled $[H_2PO_4]^-$ etching process. Dihydric phosphate was considered as the most effective agent to dissolve the iron oxide contaminant in minerals, [26, 29] and its reaction with iron oxides was gentler, thus granting better control over the etching process.

2. Experiment Section

2.1 Materials preparation

Chemicals. Ferric chloride hexahydrate ($FeCl_3 \cdot 6H_2O$, 99%), sodium sulfate (Na_2SO_4, 99%), sodium dihydrogen phosphate ($NaH_2PO_4 \cdot 2H_2O$, 99%), all the reagents were purchased from Sinopharm Chemical Reagent Co. Ltd. and used without further purification. Ultrapure distilled and deionized water was used for all solution preparations.

Fe_2O_3 Mother Crystal Synthesis. For the synthesis of pristine Fe_2O_3 nanocrystal (Sample A), an aqueous solution was first prepared by mixing 60 mL of deionized water (18 MΩ), 0.324 g ferric chloride hexahydrate (0.02 M), 0.0047g sodium sulfate (0.55 mM) in a 100-mL flat-bottomed flask. The mixture was stirred with a magnetic blender for about 10 min and then transferred into a stainless-steel autoclave with a capacity of 100 mL, sealed and heated at 220 ℃ for 5 h. When the reaction was completed, the autoclave was cooled to room temperature naturally. The brick red precipitate was centrifuged, washed several times with distilled water and absolute alcohol, and finally dried in a dry oven at 60 ℃ for 5h for further characterizations.

Fe_2O_3 Concave and Hexagonal Ring Shaped Nanocrystal Synthesis. The precursor solution was prepared by mixing 60 mL of deionized water (18 MΩ), 0.324 g ferric chloride hexahydrate (0.02 M), 0.0047g sodium sulfate (0.55 mM) and 0.00048g sodium dihydrogen phosphate (0.05 mM) for typical Fe_2O_3 concave nanocrystal (Sample B). While, 60 mL of deionized water (18 MΩ), 0.324 g ferric chloride hexahydrate (0.02 M), 0.0071g sodium sulfate (0.825 mM) and 0.00072g sodium dihydrogen phosphate (0.075 mM) for the hexagonal-hollow-ring shaped Fe_2O_3 nanocrystal (Sample C). The mixture was stirred with a magnetic blender for about 10 min and then transferred into a stainless-steel autoclave with a capacity of

100 mL, sealed and heated at 220 ℃ for 5 h. When the reaction was completed, the samples were cooled, centrifuged, cleaned and reserved.

2.2 Characterization

The crystal structures, morphologies, and chemical compositions of the as-prepared samples were studied using X-ray diffraction (XRD, X'Pert Pro MPD system, CuKα), scanning electron microscopy (SEM, Hitachi S-4800), transmission electron microscopy (TEM, JEOL 2100F, 200 kV). The surface areas of the catalysts were calculated by N_2 adsorption-desorption isotherms using a TriStar 3000 with the Brunauer-Emmett-Teller (BET) methods. The electrochemical impedance spectral (EIS) measurements were carried out on an electrochemical workstation (Zahner, IM6). For Zeta potential measurements, a commercial dynamic light scattering instrument (DLS, Malvern Nano zetasizer 90) has been chosen in this work. X-ray photo-electron spectroscope (XPS, ESCALAB 250XI) measurements were also carried out for the analysis of surface element composition.

2.3 Photocatalytic properties

The photocatalytic activity of the as-prepared samples on the degradation of RhB in aqueous solution was evaluated by measuring the absorbance of the irradiated solution, using a spectrophotometer (Shimadzu, 3100 UV-vis-NIR). Prior to irradiation, 10 mg of photocatalyst was mixed with RhB (50 mL, with a concentration of 0.02 mM) in a 100-mL flat bottom flask and then sonicated in a cool water bath for 10 min. Afterward, the suspension was magnetically stirred in the dark for 1 h to reach a relative adsorption-desorption equilibrium, followed by the addition of 0.3 mL of hydrogen peroxide solution (H_2O_2, 30 wt %). Then the beaker was exposed to visible light irradiation with maximum illumination time up to 4 hours. During the irradiation, the suspension was magnetically stirred by using a magnetic stirrer and the reaction temperature was kept at room temperature by using a water cooling system. The suspension was subsequently illuminated by a 300 W xenon lamp (the wavelength distributes from 400 nm to 800 nm) at a ca. 30 cm distance (the optical irradiance at the sample was about 30 mW cm^{-2}). A wave filter plate (λ >420 nm) was utilized to allow visible light to transmit. At given time intervals (0.5 h), about 4 mL

aliquots were sampled and centrifuged to separate the catalyst. The dye concentration in the filtrate was analyzed by measuring the absorption intensity of RhB at 554 nm.

3. Results and discussion

Typical morphology and structure of α-Fe_2O_3 pristine nanocrystals have been discussed systemically by SEM and TEM (Fig. 1). The as-synthesized Fe_2O_3 mother crystals showed truncated hexagonal bipyramidal structure (Fig. 1a, b), [23] similar as the short axis Fe_2O_3 icositetrahedron reported in our previous work. [21] These crystals were homogeneous in shape and uniform in dimensions with an average diameter of 146 ±8 nm and an average axial length of 120 ±10 nm (50 nanoparticles were counted). All peaks in the XRD pattern (Fig. S6g) could be perfectly indexed to rhombohedral hematite (α-Fe_2O_3, JCPDS 33-0664). The peaks were sharp and no other phases were observed, indicating good crystallinity and high phase purity.

The crystallographic orientation of each exposed surface was determined through the analysis of diffraction and high resolution TEM (HRTEM) images (Fig. 1c-o). To assign the surface facets, the nanoparticles were tilted in TEM until the surface was parallel to the electron beam. When the Fe_2O_3 crystal was tilted along [001] direction, six side facets were parallel to the beam (Fig. 1c-f). The spacing of lattice planes parallel to the surface was measured to be 0.25 nm (Fig. 1e, HRTEM image of region '1' in Fig. 1c), corresponding to α-Fe_2O_3 {110} plane. The SAED pattern and HRTEM image indicated that the exposed surfaces of the sample under this condition were six equivalent {110} facets. When the crystal was tilted along [2-10] direction, there were also six side facets parallel to the electron beam (Fig. 1g-k). From the SAED pattern and HRTEM images of the selected areas (region '2' and '3' in Fig. 1g), the exposed side planes could be indexed to four equivalent {113} facets and two {110} planes. In addition, when the particle was tilted anticlockwise 30 ° from [2-10] to [-100] zone axis (Fig. 1i-o), two top surfaces became parallel to the electron beam and could be indexed as {104} planes, according to the SAED pattern and HRTEM images. Comprehensive the above analysis and according to the former reports, [21, 23, 28, 30] it could be concluded that the as-prepared Fe_2O_3 mother crystal also possess

icositetrahedron structure.

As we know, phosphate ions have been widely used as shape controller to induce anisotropic growth of hematite nanocrystals. [21, 26] And in addition, the kinetic control of the monomer concentration and the crystal growth rate were the key factors to manipulate the particle size as well as material shapes initiated from the anisotropic growth. [31, 32] Thus, in this work, concentration dependent experiments were performed to explore the influence of phosphate and sulfate ions on the growth of Fe_2O_3 polyhedrons (Fig. 2, Fig. S1-S3). When the experiment was carried out without phosphate ions, the typical Fe_2O_3 icositetrahedron was obtained (Fig. 2a). When the phosphate ions (0.025 mM) were introducing into the reaction system, the Fe_2O_3 polyhedrons maintained the hexagonal shape (Fig. 2b), but the end of the crystal disappeared and the icositetrahedron structure destroyed (Fig. 2b). The average diameter of the sample became a little larger (148±7 nm), while the average axial length of the crystal decreased apparently (105±8 nm). With the concentration of phosphate ions continuously increased (0.05 mM), the average axial length of the crystals decreased to 80±7 nm (Fig. 2c, Table 1). The end of the crystal disappeared completely, and evolved into typical concave structure (Sample B). When the concentration of phosphate ions increased to 0.075 mM, the average axial length of the crystals decreased to 58±5 nm, and the hexagonal-ring shaped iron oxides began to emerge. Varying the amount of sulfate and phosphate ions to 0.825 mM and 0.075 mM (Sample C), respectively, yielded the perfect hexagonal-ring shaped Fe_2O_3 nanostructures.

Figure 3 showed the morphology and structure investigations of the typical Fe_2O_3 concave nanocrystal. SEM and bright field TEM image at low magnification clearly revealed the concave structure and etched roughness surfaces of the as-synthesized Fe_2O_3 neiloid (Fig. 3a, b). The concave structures were observed to be 150±8 nm in diameter and about 80 nm in axial length. The typical SAED pattern ([001] direction) in Fig. 3(c) demonstrated that the Fe_2O_3 concave nanocrystal was well-crystallized with hexagonal structure. HRTEM images shown in Fig. 3(e, f) revealed that the synthesized Fe_2O_3 concave nanocrystal had six side surfaces of {110} parallel to its

[006] zone axis, similar with the Fe_2O_3 icositetrahedron (Fig. 1c-f). When the Fe_2O_3 concave crystal was tilted along the [2-10] direction (SAED, Fig. 3h), the spacing of lattice planes parallel to the surface were measured to be 0.25 nm (Fig. 3i, j, HRTEM image of region '3' and '4' in Fig. 3g), corresponding to α-Fe_2O_3 {110} plane distance.

SEM and TEM investigations of the typical Fe_2O_3 hexagonal hollow rings were shown in Figure 4. From the low magnification images, the sizes of the products were homogeneous, and more than half of them possessed hollow ring shape with diameter of 153 ± 10 nm and axial length of 58 ± 5 nm (Fig. 4a, b). From the top view of a single Fe_2O_3 ring (Fig. 4c), it could be seen that the product similar to a hexagonal ring with a central hole. The SAED pattern (Fig. 4d) indicated that the nanorings were single crystals with a ring axis of [001]. On the basis of the SAED pattern and HRTEM images (Fig. 4e, f), the external wall surfaces should be {110} planes of hexagonal hematite. Figure 4g-j displayed the side view of the sample by TEM characterization along [-100] zone axis, which showed the similar lattice structure to the Fe_2O_3 icositetrahedron (Fig. 1i-o), but compared with it, the exposed wall surfaces {104} facets were disappeared. Thus, we deduced that the growth of the typical Fe_2O_3 concave and hollow nanocrystals should be the results of oriented etching of the Fe_2O_3 icositetrahedron along the common crystallographic direction ([006] zone axis).

On the basis of our experimental results, a probable evolution mechanism of the Fe_2O_3 concave and hollow nanocrystal was proposed (Fig. 5). When the additive anions (sulfate and phosphate ions) were introduced into the reaction, with their strong affinity for Fe_2O_3 {110} planes, [26, 29] would act as a shape controller to induce the Fe_2O_3 icositetrahedron growth (Fig. 5a). The formation of Fe_2O_3 with $FeCl_3$ as source generally involves two reactions (1, 2) as follows: [21]

$$Fe^{3+} + 3H_2O \leftrightarrow Fe(OH)_3 + 3H^+ \quad (1)$$

$$2Fe(OH)_3 \leftrightarrow Fe_2O_3 + 3H_2O \quad (2)$$

$$H_2PO_4^- \leftrightarrow HPO_4^{2-} + H^+ \quad (3)$$

$$Fe_2O_3 + 6H^+ \leftrightarrow 2Fe^{3+} + 3H_2O \quad (4)$$

With the concentration of $[H_2PO_4]^-$ increased, the faintly acid of the agent released the H^+ (reaction 3), which would not only reduce the hydrolysis of Fe^{3+}, but also probably etched the formed products (reaction 4) from the end of the Fe_2O_3 icositetrahedrons (Fig. 5b). With the amount of the $[H_2PO_4]^-$ increased continuously, the Fe_2O_3 icositetrahedrons evolved to concaves and then hexagonal hollow rings (Fig. 5c-e). So, the formation mechanism of the Fe_2O_3 concave and hollow nanocrystals should be a result of the changes of the addition of NaH_2PO_4. [21, 26]

Figure 6(a) showed the absorption spectra for the typical α-Fe_2O_3 icositetrahedron, concave nanocrystal and hexagonal ring (Samples from A to C) in deionized water. All the three typical Fe_2O_3 polyhedrons almost shared the similar features of absorption, the broad band around 520 nm, which overlaps the absorption band with RhB (554 nm). While, the absorption edge of the samples exhibited various absorption spectrum characteristics with different shapes. [33] According to the interband transition formula in semiconductor near the absorption edge, the absorption coefficient (α) and optical gap (E_g) obey the following equation: [34, 35]

$$(\alpha h\nu)^2 = A(h\nu - E_g) \quad (5)$$

where A was restricted by the valence and conduction band of material and hν was the photon energy. Thus by linearly fitting on the absorption edge of the corresponding curve, the band gaps of the single crystal Fe_2O_3 polyhedrons (from Sample A to C) were obtained to be 1.92, 2.00 and 1.90 eV, respectively (upper inset of Fig. 6a), the difference of which might be ascribed to the quantum confinement effect of the α-Fe_2O_3 nanoparticles.

Table 1 showed the specific surface area (SSA) and Zeta potential (in neutral water solution, PH=7) of the different samples. With the shape of the Fe_2O_3 nanocrystals evolved from icositetrahedron, concave to hexagonal hollow ring (Sample A to C), the SSA of the sample increased from 10.31 to 12.71 m^2g^{-1}. However, the concave nanocrystal had the greatest average pore size (18.99 nm) and Zeta potential (18.7 mV), probably implied the different physical and chemical properties and better

stability than the other structures. Surface element composition measurements of the samples were carried out using an XPS setup (Fig. 6b). [36] From which we could find that the peak intensity of the adsorbed OH groups hardly any changed from sample A to C, this could be ascribed to the similar exposed {110} facets of the three typical Fe_2O_3 polyhedrons.

Figure 6c showed the changes of the RhB relative concentrations (C/C_0) as a function of irradiation time, where C was the concentration of RhB at the irradiation time t and C_0 was the initial concentration. For comparison, several control experiments were performed under similar conditions (Fig. S4a), including (1) dye + H_2O_2 (without Fe_2O_3 catalyst), (2) dye + Fe_2O_3 catalyst, (3) dye + H_2O_2 + Fe_2O_3 catalyst. However, in both situation (1) and (2), the (Photo) Fenton reaction were very slow, as compared to those obviously occurred in condition (3) that α-Fe_2O_3 catalyst and H_2O_2 were used simultaneously. It was supposed that the structural Fe^{3+} plays a key role in the heterogeneous photo-Fenton reaction via the redox cycle between Fe^{3+} to Fe^{2+} to generate hydroxyl radicals. [37, 38] Meanwhile, the addition of H_2O_2 facilitated the reaction rate of the photocatalytic on the surface of Fe_2O_3 catalyst. [39] Five times repeated trials of each sample illustrated that the sequence of the photocatalytic activities of different Fe_2O_3 polyhedrons was as follows: Sample B > Sample C> Sample A, the Fe_2O_3 concave nanocrystal possessed the most superior photocatalytic activities. Generally, this phenomenon would be attributing to the lager SSA of the concave and hollow nanoparticles. [40] But, for Sample B, the SSA was clearly not the decisive factor (Table 1). Thus, it was speculated that the reason could ascribed to the edges, corners and rough structures (‘hot spots’, which often bring a large density of atomic steps, dangling bonds etc. and possess higher energy than the crystal facets [1, 4, 41]) on the etched surfaces of the concave Fe_2O_3 polyhedrons.

The EIS measurements were carried out to further evaluate the electrochemical behaviors of the three typical Fe_2O_3 polyhedrons (Fig. S4b). The results of which showed that the impedance spectra were composed of one semicircle at high frequency (inset of Fig. S4b) and a linear part at low frequency, illustrating a typical capacitor behavior. At the high frequency region, the intercept on the real axis which

represents the equivalent series resistance (*Rs*) showed the sequence as: Sample C > Sample B > Sample A, in accordance with the specific surface area (SSA) order of the materials. So, we deduced that the '*Rs'* of the typical Fe_2O_3 polyhedrons was mainly induced by the contact resistance at the interface between the electroactive material and the current collector. [42, 43] At the low frequency region, the concave Fe_2O_3 polyhedron (Sample B) showed a more vertical curve, representing the fast ion diffusion in electrolyte and the adsorption onto the electrode surface. It facilitated the efficient access of ions between electrolyte and the electrode, and thus it would aid in the photodegradation of the RhB dyes.

Recycling capability of the Fe_2O_3 polyhedrons were evaluated by the additional degradation process of fresh RhB solution with the used catalyst from the previous runs. Fe_2O_3 polyhedrons were reused over 10 times (inset of Fig. 6d, Fig. S5) and almost retained the catalytic activity as the fresh catalyst through the process (Fig. 6d), especially the concave ones (Sample B). SEM and XRD results showed that after 10 times reaction, the morphology and crystallinity of the three typical Fe_2O_3 polyhedrons almost retained, only the surface of the samples changed a little roughness (Fig. S6). All of the results above indicated that the natural Fe_2O_3 concave nanocrystals are relatively stable and good catalyst for the removal of cationic dyes. [17, 44]

4. Conclusions

In summary, we have demonstrated a facile top-down etching method to fabricate the uniform single crystal hematite concave nanocrystals. The selective etching along [006] zone axis of the icositetrahedron was made possible by employing phosphate ions as an effective etchant. We further illustrated the versatility of this top-down etching approach by creating the typical α-Fe_2O_3 hexagonal hollow rings. When evaluated for their possible use as photocatalysts, the etched α-Fe_2O_3 concave nanocrystals with a much larger average pore size and more hot spots on the crystal surface exhibited comparative photocatalytic activities than the pristine icositetrahedrons and the subsequent hexagonal rings.

Acknowledgements

This work was supported by National Natural Science Foundation of China (Grant Nos. 51205276, 51205275, 51205274 and 61474079), China Postdoctoral Science Foundation (Grant No. 2013T60268), Science and Technology Major Project of the Shanxi Science and Technology Department（Grant No. 20121101004）, Shanxi Province Science Foundation for Youths (Grant Nos. 2012021021-5 and 2013021017-1), and Shanxi Province Foundation for Returnees (Grant No. 2013-036).

References

1 N. Tian, Z. Zhou, S. Sun, Y. Ding and Z. Wang, *Science*, 2007, **316**, 732-735.

2 M. Q. Lu, S. K. Yang, Y. P. Ho, C. L. Grigsby, K. W. Leong and T. J. Huang, *Acs Nano*, 2014, **8**, 10026-10034.

3 B. Lim, Y. J. Xiong and Y. N. Xia, *Angewandte Chemie-International Edition*, 2007, **46** 9279-9282.

4 T. Yu, D. Y. Kim, H. Zhang and Y. N. Xia, *Angewandte Chemie-International Edition*, 2011, **50**, 2773-2777.

5 Y. E. Wu, D. S. Wang, Z. Q. Niu, P. C. Chen, G. Zhou and Y. D. Li, *Angewandte Chemie-International Edition*, 2012, **51**, 12524-12528.

6 W. S. Wang, M. Dahl and Y. D. Yin, *Chemistry of Materials*, 2013, **25**, 1179-1189.

7 D. Zhou, X. R. Su, M. Boese, R. M. Wang and H. Z. Zhang, *Nano Energy*, 2014, **5**, 52-59.

8 P. Hu, S. S. Pramana, S. W. Cao, C. K. Ngaw, J. D. Lin, S. C. J. Loo and T. T. Y. Tan, *Advanced Materials*, 2013, **25**, 2567-2572.

9 Y. Liu, L. Yu, Y. Hu, C. F. Guo, F. M. Zhang and X. W. Lou, *Nanoscale*, 2012, **4**, 183-187.

10 Y. Liu, C. Y. Yu, W. Dai, X. H. Gao, H. S. Qian, Y. Hu and X. Hu, *Journal of Alloys and Compounds*, 2013, **551**, 440-443.

11 N. S. Arul, D. Mangalaraj, R. Ramachandran, A. N. Grace and J. I. Han, *Journal of Materials Chemistry A*, 2015, **3**, 15248-15258.

12 W. Wu, C. Z. Jiang and V. A. L. Roy, *Nanoscal*e, 2015, **7**, 38-58.

13 S. Yan and Q. S. Wu, *Journal of Materials Chemistry A*, 2015, **3**, 5982-5990.

14 J. M. Ma, L. Mei, Y. J. Chen, Q. H. Li, T. H. Wang, Z. Xu, X. C. Duan and W. J. Zheng, *Nanoscale*, 2013, **5**, 895-898.

15 B. Xu, D. Zheng, W. Qiu, F. Gao, S. Jiang and Q. Wang, *Biosensors & Bioelectronics*, 2015, **72**, 175-181.

16 K. Ocakoglu, T. Krupnik, B. van den Bosch, E. Harputlu, M. P. Gullo, J. D. J. Olmos, S. Yildirimcan, R. K. Gupta, F. Yakuphanoglu, A. Barbieri, J. N. H. Reek and J. Kargul, *Advanced Functional Materials*, 2014, **24**, 7467-7477.

17 W. Wu, Z. H. Wu, T. Yu, C. Z. Jiang and W. S. Kim, *Science and Technology of*

Advanced Materials, 2015, **16**, 023501.

18 J. M. Jeong, B. G. Choi, S. C. Lee, K. G. Lee, S. J. Chang, Y. K. Han, Y. B. Lee, H. U. Lee, S. Kwon, G. Lee, C. S. Lee and Y. S. Huh, *Advanced Materials*, 2013, **25**, 6250-6255.

19 X. Xu, R. Cao, S. Jeong and J. Cho, *Nano Letters*, 2012, **12**, 4988-4991.

20 J. S. Chen, T. Zhu, X. H. Yang, H. G. Yang and X. W. Lou, *Journal of the American Chemical Society*, 2010, **132**, 13162-13164.

21 P. W. Li, J. L. Ji, X. Deng, A. L. Li, J. Hu, G. Li and W. D. Zhang, *CrystEngComm*, 2015, **17**, 7283-7289.

22 S. Chen, Y. L. Xin, Y. Y. Zhou, F. Zhang, Y. R. Ma, H. H. Zhou and L. M. Qi, *Journal of Materials Chemistry A*, 2015, **3**, 13377-13383.

23 B. L. Lv, Z. Y. Liu, H. Tian, Y. Xu, D. Wu and Y. H. Sun, *Advanced Functional Materials*, 2010, **20**, 3987-3996.

24 L. L. Wang, Z. Lou, J. N. Deng, R. Zhang and T. Zhang, *Acs Applied Materials & Interfaces*, 2015, **7**, 13098-13104.

25 L. Q. Sun, X. Han, K. Liu, S. Yin, Q. L. Chen, Q. Kuang, X. G. Han, Z. X. Xie and C. Wang, *Nanoscale*, 2015, **7**, 9416-9420.

26 C. J. Jia, L. D. Sun, F. Luo, X. D. Han, L. J. Heyderman, Z. G. Yan, C. H. Yan, K. Zheng, Z. Zhang, M. Takano, N. Hayashi, M. Eltschka, M. Klaui, U. Rudiger, T. Kasama, L. Cervera-Gontard, R. E. Dunin-Borkowski, G. Tzvetkov and J. Raabe, *Journal of the American Chemical Society*, 2008, **130**, 16968-16977.

27 W. Wu, X. H. Xiao, S. F. Zhang, J. A. Zhou, L. X. Fan, F. Ren and C. Z. Jiang, Journal of Physical Chemistry C, 2010, **114**, 16092-16103.

28 M. Lin, L. Tng, T. Y. Lim, M. Choo, J. Zhang, H. R. Tan and S. Q. Bai, *Journal of Physical Chemistry C*, 2014, **118**, 10903-10910.

29 H. F. Liang, X. Xu, W. Chen, B. B. Xu and Z. C. Wang, *Crystengcomm*, 2014, **16**, 959-963.

30 T. K. Van, H. G. Cha, C. K. Nguyen, S. W. Kim, M. H. Jung and Y. S. Kang, *Crystal Growth & Design*, 2012, **12**, 862-868.

31 X. G. Peng, L. Manna, W. D. Yang, J. Wickham, E. Scher, A. Kadavanich and A. P.

Alivisatos, *Nature*, 2000, **404**, 59-61.

32 W. Liu, N. Wang, R. Wang, S. Kumar, G. S. Duesberg, H. Zhang and K. Sun, *Nano Letters*, 2011, **11**, 2983-2988.

33 Y. C. Yang, H. J. Wang, J. Whang, J. S. Huang, L. M. Lyu, P. H. Lin, S. Gwo and M. H. Huang, *Nanoscale*, 2014, **6**, 4316-4324.

34 W. Liu, R. M. Wang and N. Wang, *Applied Physics Letters*, 2010, **97**, 041916.

35 G. X. Wang, X. L. Gou, J. Horvat and J. Park, *Journal of Physical Chemistry C*, 2008, **112**, 15220-15225.

36 S. Yamamoto, T. Kendelewicz, J. T. Newberg, G. Ketteler, D. E. Starr, E. R. Mysak, K. J. Andersson, H. Ogasawara, H. Bluhm, M. Salmeron, G. E. Brown and A. Nilsson, *Journal of Physical Chemistry C*, 2010, **114**, 2256-2266.

37 W. P. Du, Q. Sun, X. J. Lv and Y. M. Xu, *Catalysis Communications*, 2009, **10**, 1854-1858.

38 M. M. Cheng, W. J. Song, W. H. Ma, C. C. Chen, J. C. Zhao, J. Lin and H. Y. Zhu, *Applied Catalysis B-Environmental*, 2008, **77**, 355-363.

39 W. P. Du, Y. M. Xu and Y. S. Wang, *Langmuir*, 2008, **24**, 175-181.

40 H. F. Liang, W. Chen, X. D. Jiang, X. Xu, B. B. Xu and Z. C. Wang, *Journal of Materials Chemistry A*, 2014, **2**, 4340-4346.

41 Y. Shang, D. Sun, Y. M. Shao, D. F. Zhang, L. Guo and S. H. Yang, *Chemistry-a European Journal*, 2012, **18**, 14261-14266.

42 C. R. Zheng, C. B. Cao, Z. Alia, J. H. Hou, *Journal of Materials Chemistry A*, 2014, **2**, 16467-16473.

43 G. Li, C. Xu, *Carbon*, 2015, **90**, 44-52.

44 X. M. Zhou, Q. L. Xu, W. Y. Lei, T. T. Zhang, X. Y. Qi, G. Liu, K. Deng and J. G. Yu, *Small*, 2014, **10**, 674-679.

Tables

Table 1. Sample parameters, specific surface area (SSA) and Zeta potential of typical iron oxides.

Samples	Diameter (nm)	Height (nm)	Surface area (m^2 g^{-1})	Total pore volume (cm^3 g^{-1})	Average pore size (nm)	Zeta potential (mV)
A	146 ±8	120 ±10	10.31	0.044	17.26	-4.3
B	150 ±8	80 ±7	11.88	0.056	18.99	18.7
C	153 ±10	58 ±5	12.71	0.059	18.53	7.9

Figures and Captions

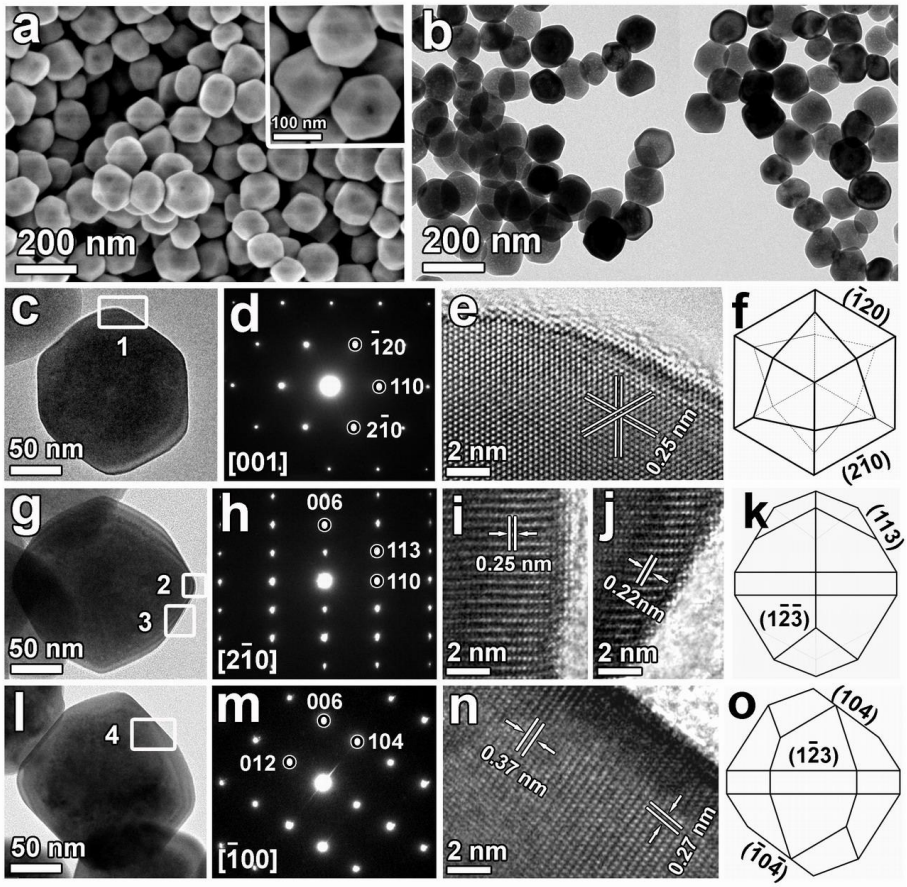

Figure 1. Typical morphology and structure of α-Fe_2O_3 icositetrahedron synthesized without $[H_2PO_4]^-$ (Sample A). (a, b) SEM and bright field TEM images; (c-f) TEM image, corresponding SAED pattern, HRTEM images and geometrical configuration pattern showing the [006] zone axis parallel to the electron beam; (g-k) TEM image, corresponding SAED pattern, HRTEM images and geometrical configuration pattern showing the {113} and {110}surfaces parallel to the electron beam; (l-o) TEM image, corresponding diffraction pattern, HRTEM images and geometrical configuration pattern showing the {104} surfaces parallel to the electron beam when the same particle was tilted anticlockwise 30 °.

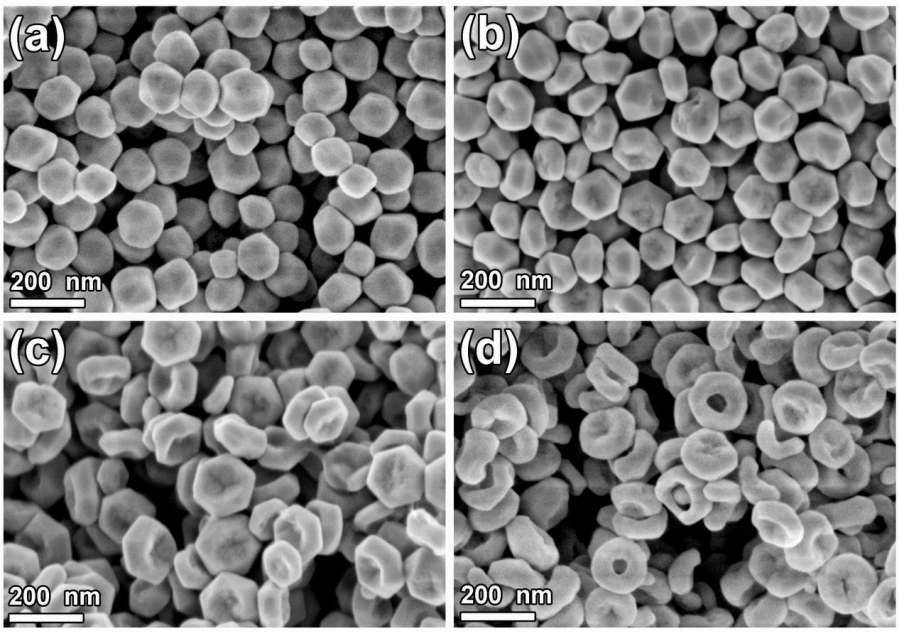

Figure 2. SEM images of shape evolution of α-Fe_2O_3 nanocrystals (from icositetrahedron, concave to hexagonal ring) at different $[H_2PO_4]^-$ concentration: (a) 0, (b) 0.025, (c) 0.05 and (d) 0.075 mM, respectively.

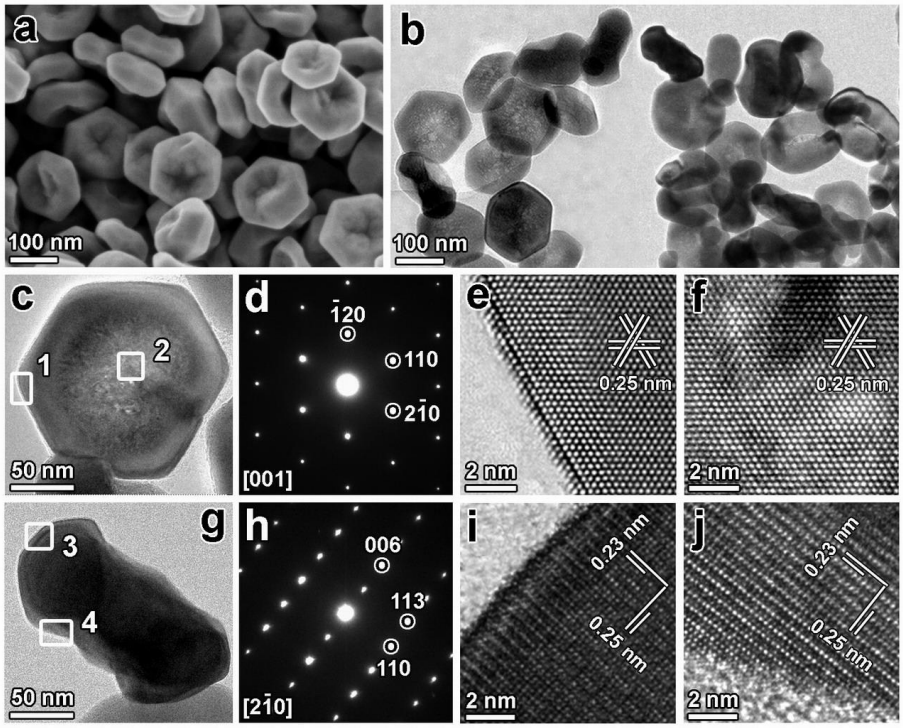

Figure 3. Typical morphology and structure of α-Fe_2O_3 concave nanocrystal. (a, b) SEM and bright field TEM images; (c-f) TEM image, corresponding SAED pattern and HRTEM images along [001] zone axis; (g-k) TEM image, corresponding diffraction pattern and HRTEM images along [2-10] zone axis.

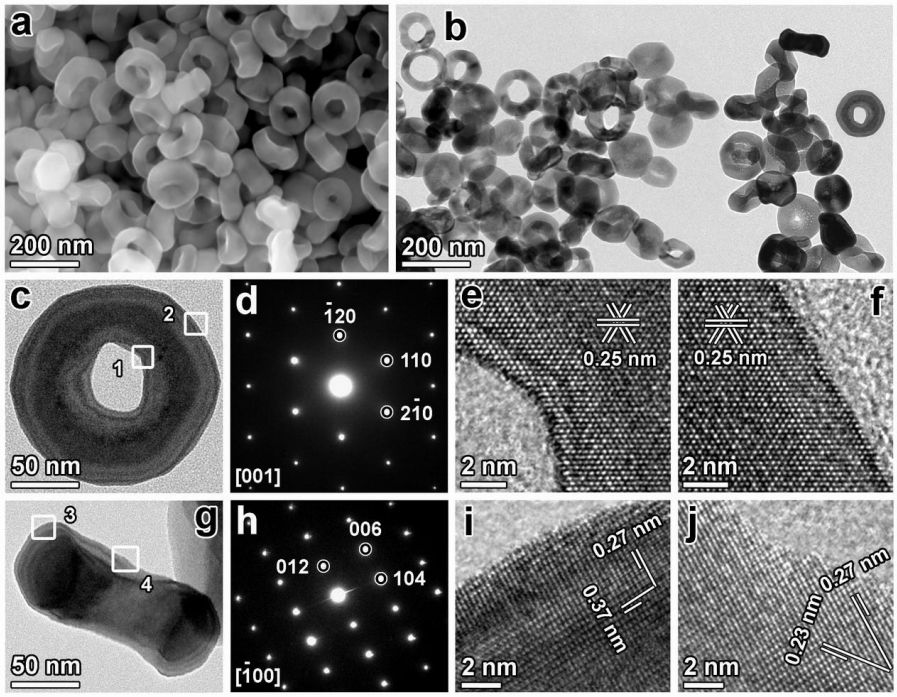

Figure 4. Typical morphology and structure of α-Fe_2O_3 hexagonal ring. (a, b) SEM and bright field TEM images; (c-f) TEM image, corresponding SAED pattern and HRTEM images along [001] zone axis; (g-k) TEM image, corresponding diffraction pattern and HRTEM images along [-100] zone axis.

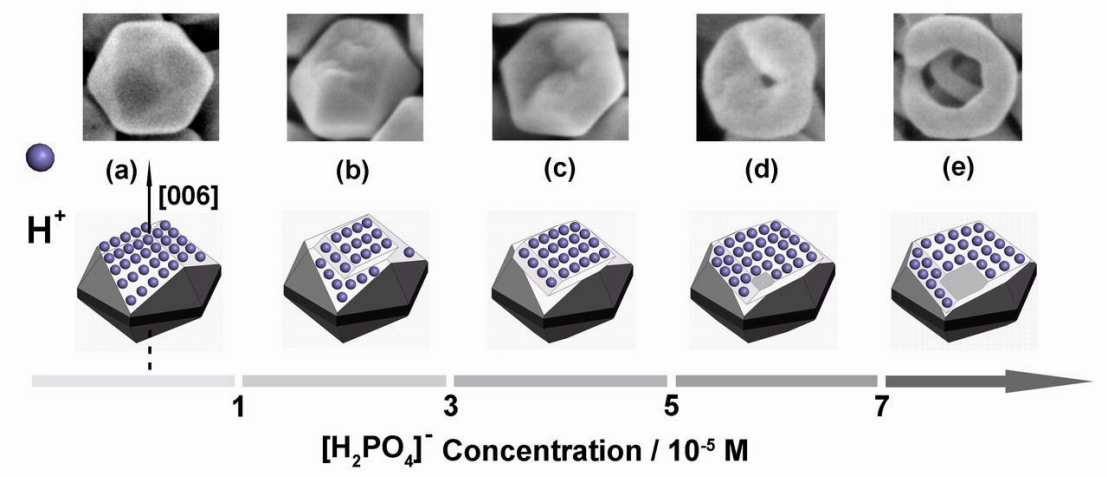

Figure 5. Schematic diagram showing the axial etching of Fe_2O_3 nanocrystal from icositetrahedron, concave to hexagonal ring with the $[H_2PO_4]^-$ concentration increasing.

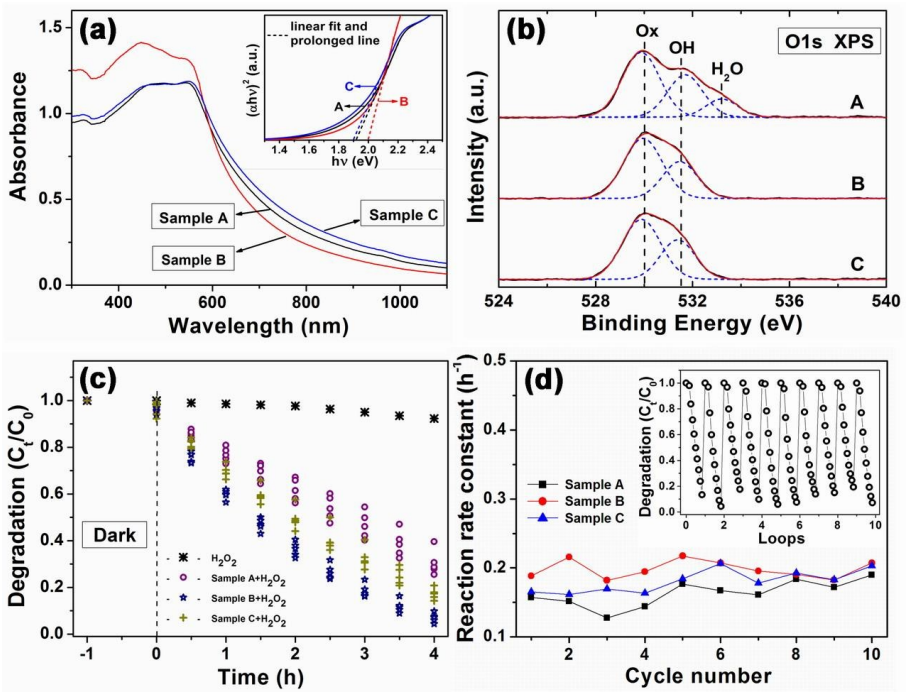

Figure 6. The optical properties of the as-prepared samples: (a) Absorption spectra for α-Fe_2O_3 polyhedrons with various shapes (Samples from A to C), the inset above shows linear fits (dashed lines) of the $(\alpha h\nu)^2$-hν curves calculated from the absorption spectra; (b) O 1s XPS spectra of samples from A to C, the experimental data are shown as solid black lines and the results of the peak fitting are shown as short dash. (c) The changes of the RhB relative concentrations (C/C_0) as a function of irradiation time, each degradation process have been repeated for 5 times. (d) Recycling capability of different Fe_2O_3 polyhedrons on the degradation process of RhB, each sample was reused over 10 times; the inset above shows the cyclic degradation process of RhB with the α-Fe_2O_3 concave nanocrystal (Sample B).

"Table of Contents" Graphic:

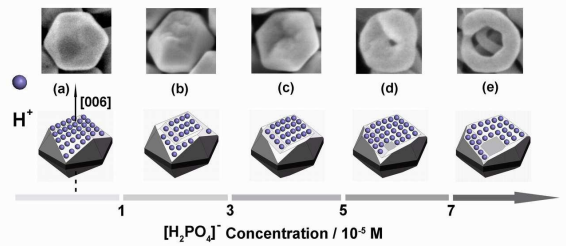

Top-Down Etching Synthesis of α-Fe_2O_3 Concave and Hollow Nanocrystals